

¹ Study of the multi-strange resonance $\Xi(1530)^0$ production
² with ALICE at the LHC energies

³ Jihye Song

4 Contents

5	List of Figures	4
6	List of Tables	6
7	1 The physics of relativistic heavy-ion collisions	7
8	1.1 Standard model	7
9	1.2 Quantum Chromo-Dynamics	7
10	1.3 Heavy Ion Collisions	7
11	2 Production of resonance with strangeness	7
12	2.1 Resonance with strangeness	7
13	3 Theoretical models	7
14	3.1 Thermal statistical model	7
15	3.1.1 Calculations	9
16	3.1.2 Results	9
17	3.1.3 Comparison with data	11
18	3.2 UrQMD	11
19	4 A Large Ion Collider Experiment at the LHC	11
20	4.1 The Large Hadron Collider	12
21	4.2 The ALICE project	12
22	4.2.1 ALICE detector	12
23	4.2.2 Data Acquisition (DAQ) and trigger system	12
24	4.2.3 ALICE offline software frame work	12
25	5 Measurement of $\Xi(1530)^0$ production in p-Pb and Pb-Pb	12
26	5.1 $\Xi(1530)^0$ -reconstruction	13
27	5.1.1 Data sample and event selection	13
28	5.1.2 Track and topological selection	16
29	5.1.3 Particle identification	19
30	5.1.4 Signal extraction	21
31	5.2 Efficiency correction	29
32	5.3 Corrected p_T -spectra	32
33	5.4 Systematic uncertainties	34
34	5.5 $\Xi(1530)^0$ transverse momentum spectra	39
35	6 Results	42
36	6.1 dN/dy and $\langle p_T \rangle$	42
37	6.2 Particle yield ratios	42

38	6.2.1	Comparison with other resonances	42
39	6.2.2	Comparison with models	42
40	References		42

41 **List of Figures**

42 1	Ratio of baryonic and mesonic resonances over their stable partner as a function of temperature.	10
44 2	Ratio of resonances over their stable partner as a function of $\sqrt(s)$	11
45 3	Vertex-z coordinate distribution of the accepted events in full multiplicity range 0-100%. The red dashed line indicates vertex cut	15
47 4	Multiplicity distribution of accepted events in percentile. The each color and labels define the four intervals in which the analysis is performed.	15
49 5	Sketch of the decay modes for Ξ^{*0} (right) and depiction of the track and topological selection criteria.	17
51 6	TPC dE/dx as function of transverse momentum for total (top) and selected first emitted π in 3σ (bottom)	19
53 7	TPC dE/dx as function of transverse momentum for total (top) and selected second emitted π in 3σ (bottom)	19
55 8	TPC dE/dx as function of transverse momentum for total (top) and selected last emitted π in 3σ (bottom)	20
57 9	TPC dE/dx as function of transverse momentum for total (top) and selected proton in 3σ (bottom)	20
59 10	The $\Xi^\mp\pi^\pm$ invariant mass distribution (Same-event pairs) in $1.8 < p_T < 2.2 \text{ GeV}/c$ and for the multiplicity class 20-40%. The background shape, using pairs from different events (Mixed-event background), is normalised to the counts in $1.49 < M_{\Xi\pi} < 1.51 \text{ GeV}/c^2$ and $1.56 < M_{\Xi\pi} < 1.58 \text{ GeV}/c^2$	21
63 11	The $\Xi^\mp\pi^\pm$ invariant mass distribution (Same-event pairs) in $3.0 < p_T < 3.5 \text{ GeV}/c$ and for the centrality class 0-10%. The background shape, using pairs from different events (Mixed-event background), is normalised to the counts in $1.49 < M_{\Xi\pi} < 1.51 \text{ GeV}/c^2$ and $1.56 < M_{\Xi\pi} < 1.58 \text{ GeV}/c^2$	22
67 12	The invariant mass distribution after subtraction of the mixed-event background in p-Pb collisions. The solid curve represents the combined fit, while the dashed line describes the residual background.	23
70 13	The invariant mass distribution after subtraction of the mixed-event background in Pb-Pb collisions. The solid curve represents the combined fit, while the dashed line describes the residual background.	24
73 14	σ fit parameters as a function of $p_{T\text{in MB}}$ in p-Pb collisions (top) and in Pb-Pb collisions (bottom).	26
75 15	$\Xi(1530)^0$ -mass obtained from fit of the Voigtian peak as a function of $p_{T\text{in}}$ each multiplicity classes in p-Pb collisions (top) and the different centrality classes in Pb-Pb (bottom).	27
78 16	$\Xi(1530)^0$ -raw spectra obtained from fit of the Voigtian peak and a polynomial residual background for different multiplicities in p-Pb collisions (top) and Pb-Pb collisions (bottom). Only the statistical error is reported.	28

81	17	$\Xi(1530)^0$ -raw spectra obtained from fit of the Voigtian peak and a poly-				
82		nomial residual background for different multiplicities. Only the statistical				
83		error is reported.				29
84	18	Real corrected $\Xi(1530)^0$ spectrum (black) for the minimum bias with Levy				
85		fit (black curve). Also shown are the unweighted generated (blue) and re-				
86		constructed (red) $\Xi(1530)^0$ spectra.				30
87	19	Efficiency as a function of p_T in minimum bias events in p–Pb collisions. . .				31
88	20	Efficiency as a function of p_T in different centrality classes in Pb–Pb collisions				32
89	21	Corrected p_T -spectra of $\Xi(1530)^0$ in NSD and different multiplicity classes				
90		in p–Pb collisions.				33
91	22	Corrected p_T -spectra of $\Xi(1530)^0$ in different centrality classes in Pb-Pb				
92		collisions.				33
93	23	Summary of the contributions to the systematic uncertainty in minimum bias				
94		events in p–Pb collisions. The dashed black line is the sum in quadrature of				
95		all the contributions.				37
96	24	Systematic uncertainties for each multiplicity classes in p–Pb collisions. . .				37
97	25	Summary of the contributions to the systematic uncertainty in minimum bias				
98		events in Pb–Pb collisions. The dashed black line is the sum in quadrature				
99		of all the contributions.				38
100	26	Systematic uncertainties for each multiplicity classes.				38
101	27	Corrected yields as function of p_T in NSD events and multiplicity dependent				
102		event classes in p–Pb collision system. Statistical uncertainties are presented				
103		as bar and systematical uncertainties are plotted as boxes.				40
104	28	Corrected yields as function of p_T in different centrality classes in Pb–Pb col-				
105		lision system. Statistical uncertainties are presented as bar and systematical				
106		uncertainties are plotted as boxes.				41

¹⁰⁷ **List of Tables**

¹⁰⁸	1	Parameters used in the thermal-model calculations.	8
¹⁰⁹	2	Properties of particles used in the ratio calculations.	9
¹¹⁰	3	Difference of mass (ΔM), baryon number (ΔB), strangeness (ΔS) and charge (ΔQ) of the ratios. The values of the slopes needs to be checked!!!! .	11
¹¹¹	4	Number of events at different selection stages.	14
¹¹²	5	Number of accepted and analysed events per multiplicity interval	16
¹¹³	6	Track selections common to all decay daughters and primary track selections applied to the charged pions from decays of Ξ^{*0}	16
¹¹⁴	7	Topological and track selection criteria.	17
¹¹⁵	8	Summary of the systematic uncertainties on the differential yield, $d^2N/(dp_T dy)$. Minimum and maximum values in all p_T intervals and multiplicity classes in p–Pb, centrality classes in Pb–Pb are shown for each source.	39
¹¹⁶			
¹¹⁷			
¹¹⁸			
¹¹⁹			

120 **1 The physics of relativistic heavy-ion collisions**

121 This test for references [1]

122 **1.1 Standard model**

123 **1.2 Quantum Chromo-Dynamics**

124 **1.3 Heavy Ion Collisions**

125 **2 Production of resonance with strangeness**

126 **2.1 Resonance with strangeness**

127 **3 Theoretical models**

128 **3.1 Thermal statistical model**

129 The statistical-thermal model has proved extremely successful in applications to relativistic
130 collisions of both heavy ions and elementary particles. In light of this success, THERMUS,
131 a thermal model analysis package, has been developed for incorporation into the object-
132 oriented ROOT framework [2].

133

134 There are three types of statistical-thermal models in explaining data in high energy nu-
135 clear physics and THERMUS treats the system quantum numbers B (baryon number), S
136 (strangeness) and Q (charge) within three distinct formalisms:

137 1. **Grand-Canonical Ensemble:** Because the hot dense matter produced in nucleus-
138 nucleus collisions is large enough, this ensemble is the most widely used in applications
139 to heavy-ion collisions, in which the quantum numbers are conserved on average.

140 2. **Fully-Canonical Ensemble:** In which B, S and Q are each exactly conserved and
141 this ensemble used in high-energy elementary collisions such as pp, p \bar{p} and e $^-$ e $^+$
142 collisions.

143 3. **Strangeness-Canonical Ensemble:** In small systems or at low temperatures, a
144 canonical treatment leads to a suppression of hadrons carrying non-zero quantum
145 numbers, since these particles have to be created in pairs and the resulting low
146 production of strange particles requires a canonical treatment of strangeness.

147 In order to calculate the thermal properties of a system, one starts with an evaluation
148 of its partition function. The form of the partition function obviously depends on the
149 choice of ensemble. In the present analysis the strangeness-canonical ensemble used and
150 the statistical-thermal model requires six parameters as input: the chemical freeze-out

151 temperature T , baryon and charge chemical potentials μ_B and μ_Q respectively, canonical
152 or correlation radius, R_C ; the radius inside which strangeness is exactly conserved and the
153 fireball radius R . An additional strangeness saturation factor γ_S has been used as indicator
154 of a possible departure from equilibrium and $\gamma_S = 1.0$ corresponds to complete strangeness
155 equilibration.

156 The volume dependence cancels out when studying the particle ratios as well as strangeness
157 canonical equivalent to grand canonical formalism if $\Delta S = 0$ in the ratios and γ_S also can-
158 cels out. Parameters used in the analysis listed in Table 1. The μ_B parameter taken from
159 the Ref. [3].

Table 1: Parameters used in the thermal-model calculations.

Parameter	Value
T (MeV)	varied (see text)
μ_B (MeV)	$9.2 \times 10^{-2}????$
μ_Q (MeV)	0.0
γ_S	1.0

161 **3.1.1 Calculations**

162 *Concept:*

163 In order to calculate the particle ratios within strangeness canonical formalism of THER-
 164 MUS, temperature varied between 60 MeV to 180 MeV and particle yields extracted for
 165 each temperature value and then primary particle ratios calculated for each case.

166

167 *Feed-Down Correction:*

168 Since the particle yields measured by the detectors in collision experiments include feed-
 169 down from heavier hadrons and hadronic resonances, the primordial hadrons are allowed to
 170 decay to particles considered stable by the experiment before model predictions are com-
 171 compared with experimental data. In the analysis only Λ particles counted as stable (do not
 172 allowed to decay) so there is no feed-down contribution from these particles to the other
 173 ratios.

174

175

176 Properties of studied particles and their particle ratios listed in Table 2 and Table 3,
 177 respectively.

Table 2: Properties of particles used in the ratio calculations.

Particle	Δ^{++}	p	K^{*0}	K^0	K^+	Λ^*	Λ	Σ^{*+}	Σ^+	Σ^0
Mass (MeV/c^2)	1232	938.27	895.92	497.61	493.67	1519.5	1115.68	1382.8	1189.37	1192.6
Width (MeV/c^2)	120	–	50.7	–	–	15.6	–	37.6	–	–
$c\tau$ (fm)	1.6	–	3.9	–	–	12.6	–	5.51	–	–
Ang. Momentum (J)	3/2	1/2	1	1	0	3/2	1/2	3/2	1/2	1/2
Isospin (I)	3/2	1/2	1/2	1/2	1/2	0	0	1	1	1
Parity (P)	+1	+1	-1	-1	0	-1	+1	+1	+1	+1
Strangeness (S)	0	0	1	1	1	-1	-1	-1	-1	-1
Baryon Number (B)	1	1	0	0	0	1	1	1	1	1
Decay Channel	$p\pi^+$	–	π^-	–	$\mu^+\nu_\mu$	pK^-	$p\pi^-$	$\Lambda\pi^+$	$p\pi^0$	$\Lambda\gamma$
Branching Ratio (%)	~ 100	–	~ 66.7	–	~ 63.54	~ 45	~ 63.9	~ 87	~ 51.6	~ 100
Q-Value(MeV/c^2)	154.16	–	262.68	–	–	87.55	37.84	127.55	111.53	76.96

178

179

180 **3.1.2 Results**

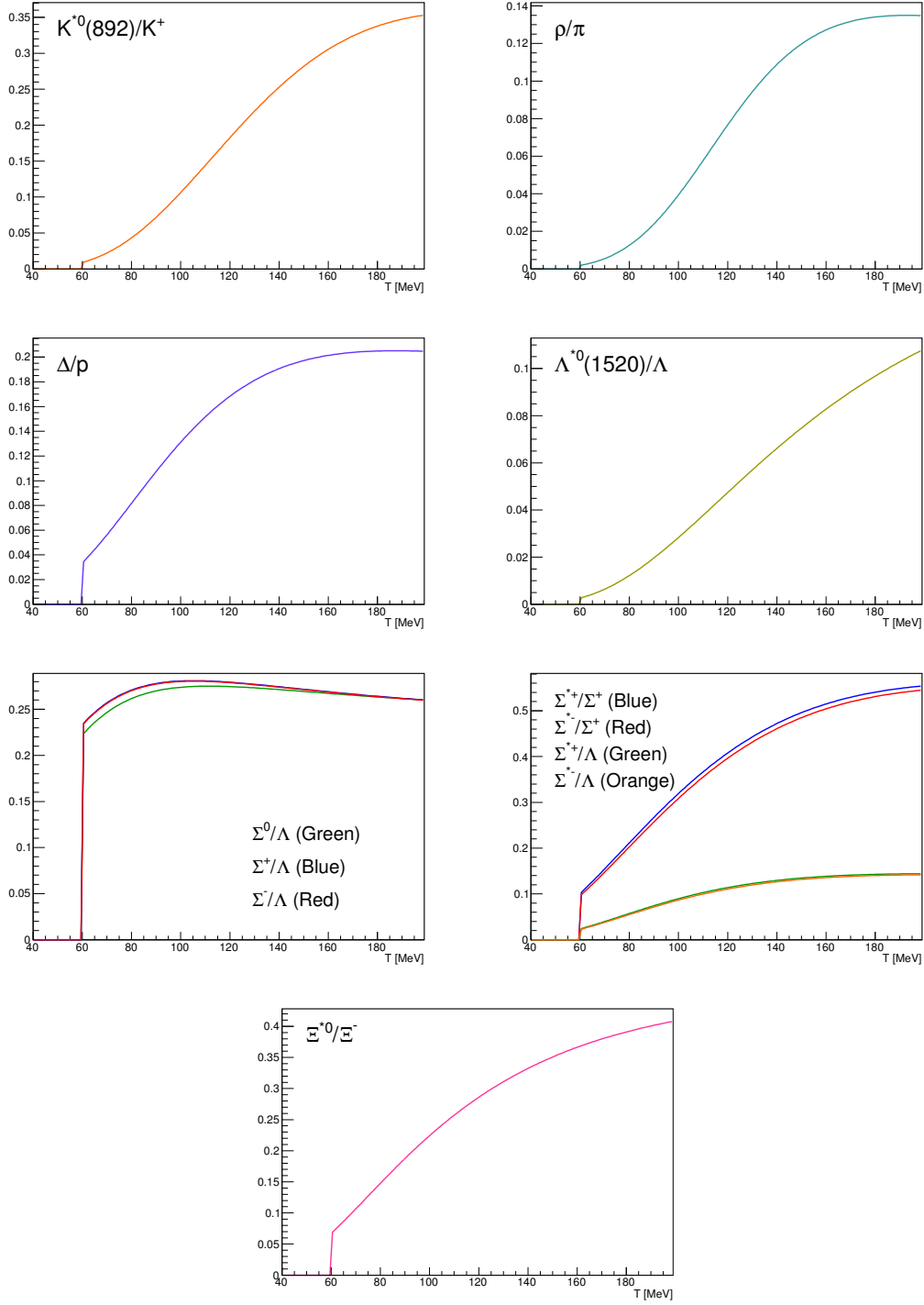


Figure 1: Ratio of baryonic and mesonic resonances over their stable partner as a function of temperature.

Table 3: Difference of mass (ΔM), baryon number (ΔB), strangeness (ΔS) and charge (ΔQ) of the ratios. The values of the slopes needs to be checked!!!!

Particle	Δ^{++}/p	K^*/K^+	Λ^*/Λ	Σ^{*+}/Λ	Σ^{*+}/Σ^0	Σ^0/Λ	Σ^{*+}/Σ^+	Ξ^{*0}/Ξ^-
ΔM (MeV/ c^2)	293.8	402.25	403.82	267.12	190.16	76.96	193.43	210.49
ΔB	0	0	0	0	0	0	0	0
ΔS	0	0	0	0	0	0	0	0
ΔQ	+1	-1	0	+1	0	+1	0	-1
Slope (%) per MeV ????????	0.19	0.76	0.98	0.25	-	-0.08	0.37	0.42

181 3.1.3 Comparison with data

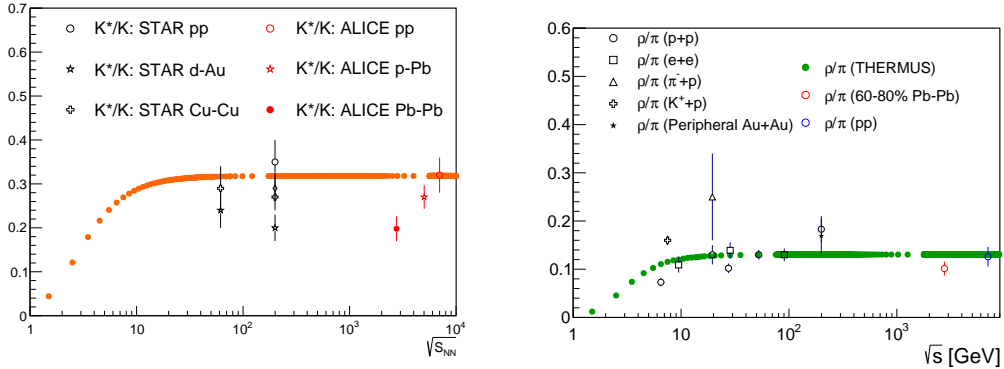


Figure 2: Ratio of resonances over their stable partner as a function of $\sqrt{(s)}$.

182 3.2 UrQMD

183 4 A Large Ion Collider Experiment at the LHC

184 ALICE (A Large Ion Collider Experiment) has been collecting data during the whole first
 185 phase of the Large Hadron Collider operations, from its startup on the 23 November 2009
 186 to the beginning of the first long technical shutdown in February 2013. During the first
 187 three years of operations LHC provided pp collisions at 0.9, 2.76, 7 and 8 TeV, Pb?Pb
 188 collisions at 2.76A TeV and finally p?Pb collisions at 5.02 TeV. The first section of this
 189 chapter focuses on the LHC performance during this phase and includes details on the
 190 accelerator parameters that allow the LHC to perform as a lead ion collider. A detailed
 191 description of the ALICE detector follows in the section 2.2. ALICE has been designed and

192 optimized to study the high particle-multiplicity environment of ultra-relativistic heavy-ion
193 collisions and its tracking and particle identification performance in Pb-Pb collisions are
194 discussed. The attention is drawn in particular on the central barrel detectors. Section
195 2.3 de- scribes the ALICE Data Acquisition (DAQ) system, that also embeds tools for the
196 online Data Quality Monitoring (DQM). The final part of the chapter is dedicated to the
197 offline computing and reconstruction system based on the GRID framework.

198 4.1 The Large Hadron Collider

199 The Large Hadron Collider (LHC) [57], [58] is a two-ring-superconducting hadron accel-
200 erator and collider installed in the 26.7 Km tunnel that hosted the LEP ma- chine and it
201 completes the CERN accelerator complex together with the PS and SPS, among the others
202 shown in fig. 2.1. Four main experiments are located in four different interaction points
203 along its circumference. ATLAS and CMS, the biggest ones, are multi-purpose detectors
204 built to discover the Higgs boson and hints of new physics beyond the Standard Model.
205 LHCb is dedicated to the physics of the flavour, focusing on the study CP-violation using B
206 meson decay channels. The phenomena that these three experiments aim to observe have
207 production cross sec- tion of the order of a hundred of pb or lower, therefore a large number
208 of collision events is required to the machine in order to fulfill the LHC pp physics program.
209 ALICE, on the contrary, is dedicated to the physics of Quark Gluon Plasma through the
210 observation of high-energy heavy-ion collisions, although a shorter physics pro- gram with
211 pp collisions has been carried out.

212 4.2 The ALICE project

213 4.2.1 ALICE detector

214 4.2.2 Data Acquisition (DAQ) and trigger system

215 4.2.3 ALICE offline software frame work

216 5 Measurement of $\Xi(1530)^0$ production in p–Pb and Pb–Pb

217 The measurement of resonance production in p–Pb collisions helps to disentangle cold
218 nuclear matter effects from genuine hot medium effects and contribute to the study of
219 the system size dependence of re-scattering in the hadronic phase. And the measurement
220 in ultra-relativistic heavy-ion collisions such as Pb–Pb collisions, provide information on
221 the properties of hadronic medium and different stage of its evolution. In order to study
222 the particle production mechanism in the hadronic phase between the chemical and ki-
223 netic freeze-out, the $\Xi(1530)^0$ resonance production at mid-rapidity($-0.5 < y_{\text{CMS}} < 0$) is
224 measured in p–Pb collisions $\sqrt{s_{\text{NN}}} = 5.02$ TeV and in Pb–Pb collisions with $|y| < 0.5$ at
225 $\sqrt{s_{\text{NN}}} = 2.76$ TeV with the ALICE experiment, via the reconstruction of its hadronic decay
226 into $\Xi\pi$.

227 **5.1 $\Xi(1530)^0$ -reconstruction**

228 The Ξ^{*0} production in p–Pb and Pb–Pb collisions at mid-rapidity has been studied in dif-
229 ferent multiplicity classes, from very central to peripheral collisions. The analysis strategy
230 is based on the invariant mass study of the reconstructed pairs (referred to as the candi-
231 dates) whose provenance could be the decay of a Ξ^{*0} baryon into charged particles. The
232 decay products (also called daughters in the text) are identified as oppositely charged Ξ and
233 π among the tracks reconstructed in the central barrel. The event selection, track selec-
234 tion and the particle identification strategy is described. The raw signal yield is extracted
235 by fitting the background-subtracted invariant mass distribution in several transverse mo-
236 mentum intervals. In order to extract the p_T -dependent cross section, these yields are
237 corrected for efficiency. The p_T -dependent correction due to the detector acceptance and
238 reconstruction efficiency, $(\text{Acc} \times \epsilon_{rec})(pt)$, is computed from a Monte Carlo simulation.
239 The absolute normalisation is then performed, by dividing for the number of the events in
240 each multiplicity and centrality classes.

241 **5.1.1 Data sample and event selection**

242 A description of the ALICE detector and of its performance during the LHC Run 1 (2010–
243 2013) can be found in [4, 5]. The data sample in the analysis from Pb–Pb collisions with
244 energy of $\sqrt{s_{\text{NN}}}=2.76$ obtained during 2011 and the sample of p–Pb run at $\sqrt{s_{\text{NN}}}=5.02$
245 TeV was recorded in 2013.

246 Due to the asymmetric energies of the proton (4 TeV) and lead ion (1.57 A TeV) beams,
247 the centre-of-mass system in the nucleon-nucleon frame is shifted in rapidity by $\Delta y_{\text{NN}} =$
248 0.465 towards the direction of the proton beam with respect to the laboratory frame of
249 the ALICE detector [6]. For the analysed p–Pb data set, the direction of the proton beam
250 was towards the ALICE muon spectrometer, the so-called “C” side, standing for negative
251 rapidities; conversely, the Pb beam circulated towards positive rapidities, labelled as “A”
252 side in the following. The analysis in this paper was carried out at midrapidity, in the
253 rapidity window $-0.5 < y_{\text{CMS}} < 0$.

254 The minimum-bias trigger during the p–Pb run was configured to select events by
255 requiring a logical OR of signals in V0A and V0C [5], two arrays of 32 scintillator detectors
256 covering the full azimuthal angle in the pseudo-rapidity regions $2.8 < \eta_{\text{lab}} < 5.1$ and
257 $-3.7 < \eta_{\text{lab}} < -1.7$, respectively [7]. In the data analysis it was required to have a
258 coincidence of signals in both V0A and V0C in order to reduce the contamination from
259 single-diffractive and electromagnetic interactions. This left only Non-Single Diffractive
260 (NSD) events, which amount for a total of 109.3 million events, in the Minimum-Bias
261 sample(~ 111.1 million events) corresponding to an integrated luminosity of about 50
262 μb^{-1} . Out of this sample in p–Pb collision events, 93.9×10^6 events satisfy the following
263 selection criteria and have been actually used for the analysis.

264 The Pb–Pb collisions data sample was selected by online centrality trigger requiring a
265 signal in the forward V0 detectors[8] to record enhanced data in central collision. The data

266 consists of 24.8×10^6 most central collisions (0-10%), 21.8×10^6 semi-central collisions
 267 (10-50%) and 3.5×10^6 minimum-bias trigger (0-90%).

- 268 • Events with z-coordinate of primary vertex (V_z) falling within ± 10 cm from the
 269 interaction point
- 270 • Rejection of pile-up event
- 271 • Requiring primary tracks to have at least one hit in one of the two innermost layers
 272 of the ITS (silicon pixel detector, SPD)
- 273 • p–Pb: multiplicity ranges in percentile (V0A): 0-20%, 20-40%, 40-60%, 60-100% and
 274 MB(0-100%)
- 275 • Pb–Pb: centrality classes (V0A and V0C): 0-10%, 10-40%, 40-80% and MB (0-80%)

276 The distribution of the vertex z position of the accepted events is reported in fig. 3.
 277 Events with $|V_z| < 10$ cm have been used to ensure a uniform acceptance in the central
 278 pseudo-rapidity region, $|\eta| < 0.8$, where the analysis is performed. This cut reduces the
 279 total number of events to 97.5×10^6 , that is the $\sim 87.8\%$ of the initial sample. The number
 280 of events before and after each event selection stages are written in Table 4. Fig. 4
 281 shows the multiplicity distribution of the accepted events divided in bins of percentile.
 282 The each colours on the histogram indicate the multiplicity ranges used in this analysis.
 283 Corresponding events for each multiplicity range are in Table 5.

Event selection stage	number of events	percentage
Original number of events	111.1×10^6	100.0%
Number of triggered events (kINT7)	109.3×10^6	98.4%
Events after PV position cut ($ V_z < 10$ cm)	97.5×10^6	87.8%
Events after reject pile-up	94.5×10^6	85.1%
Events after number of SPD cluster cut (≥ 1)	93.9×10^6	84.5%

Table 4: Number of events at different selection stages.

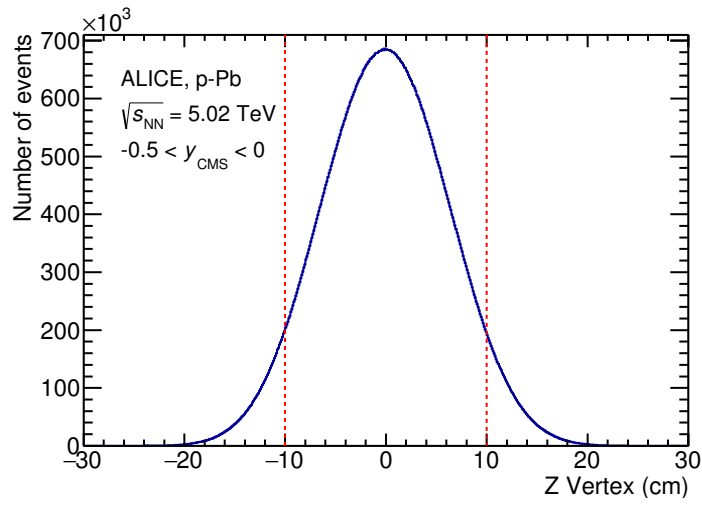


Figure 3: Vertex-z coordinate distribution of the accepted events in full multiplicity range 0-100%. The red dashed line indicates vertex cut

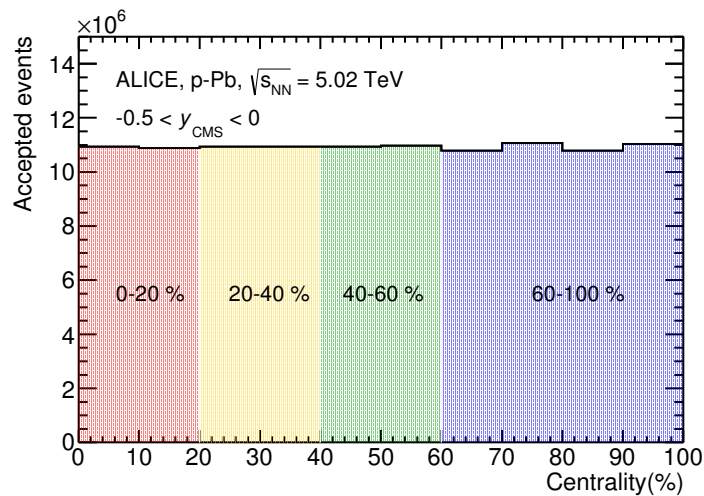


Figure 4: Multiplicity distribution of accepted events in percentile. The each color and labels define the four intervals in which the analysis is performed.

multiplicity	number of events
0-20%	21.82×10^6
20-40%	21.86×10^6
40-60%	21.91×10^6
60-100%	43.68×10^6

Table 5: Number of accepted and analysed events per multicity interval

284 5.1.2 Track and topological selection

285 In comparison with the Ξ^{*0} analysis carried out in pp collisions at $\sqrt{s} = 7$ TeV [9], track
 286 and topological selections were revised and adapted to the p–Pb dataset. Pions from strong
 287 decays of Ξ^{*0} were selected according to the criteria for primary tracks. As summarized
 288 in Table 6, all charged tracks were selected with $p_T > 0.15$ GeV/c and $|\eta_{\text{lab}}| < 0.8$, as
 289 described in Ref. [5]. The primary tracks were chosen with the Distance of Closest Approach
 290 (DCA) to PV of less than 2 cm along the longitudinal direction (DCA_z) and lower than $7\sigma_r$
 291 in the transverse plane (DCA_r), where σ_r is the resolution of DCA_r . The σ_r is strongly
 292 p_T -dependent and lower than 100 μm for $p_T > 0.5$ GeV/c [5]. To ensure a good track
 293 reconstruction quality, candidate tracks were required to have at least one hit in one of the
 294 two innermost layers (SPD) of the ITS and to have at least 70 reconstructed points in the
 295 Time Projection Chamber (TPC), out of a maximum of 159. The Particle IDentification
 296 (PID) criteria for all decay daughters are based on the requirement that the specific energy
 297 loss (dE/dx) is measured in the TPC within three standard deviations (σ_{TPC}) from the
 expected value (dE/dx_{exp}), computed using a Bethe-Bloch parametrization [5].

Common track selections	$ \eta_{\text{lab}} $	< 0.8
	p_T	> 0.15 GeV/c
	PID $ (\text{d}E/\text{d}x) - (\text{d}E/\text{d}x)_{\text{exp}} $	< 3 σ_{TPC}
Primary track selections	DCA_z to PV	< 2 cm
	DCA_r to PV	< $7\sigma_r$ - $10\sigma_r$ (p_T)
	number of SPD points	≥ 1
	number of TPC points	> 70
	χ^2 per cluster	< 4

Table 6: Track selections common to all decay daughters and primary track selections applied to the charged pions from decays of Ξ^{*0} .

298
 299 Since pions and protons from weak decay of Λ ($c\tau = 7.89$ cm [10]) and pions from weak
 300 decay of Ξ^- ($c\tau = 4.91$ cm [10]) are produced away from the PV, specific topological and
 301 track selection criteria, as summarized in Table 7, were applied [11, 9, 12].

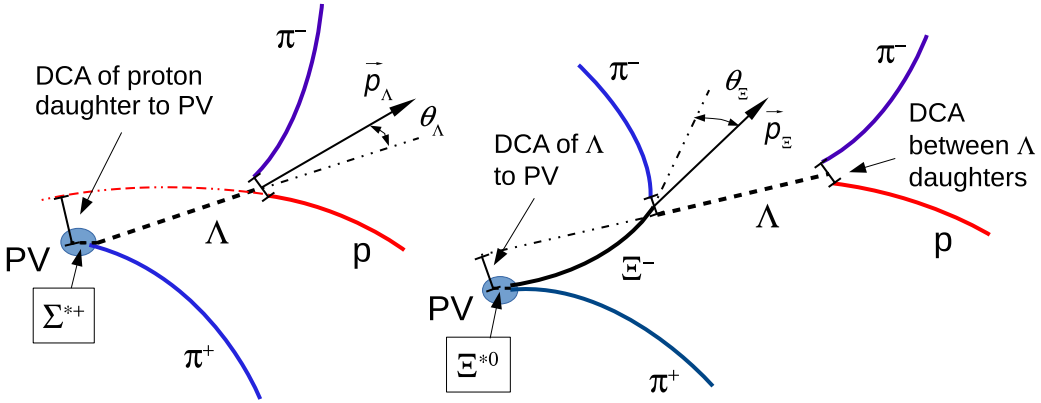


Figure 5: Sketch of the decay modes for Ξ^{*0} (right) and depiction of the track and topological selection criteria.

Topological cuts	p-Pb	Pb-Pb
DCA _r of Λ decay products to PV	> 0.06 cm	> 0.11 cm
DCA between Λ decay products	< 1.4 cm	< 0.95 cm
DCA of Λ to PV	> 0.015 cm	> 0.06
$\cos\theta_\Lambda$	> 0.875	> 0.998
$r(\Lambda)$	$0.2 < r(\Lambda) < 100$ cm	$0.2 < r(\Lambda) < 100$ cm
$ M_{p\pi} - m_\Lambda $	$< 7 \text{ MeV}/c^2$	$< 7 \text{ MeV}/c^2$
DCA _r of pion (from Ξ^-) to PV	> 0.015 cm	> 0.035 cm
DCA between Ξ^- decay products	< 1.9 cm	< 0.275
$\cos\theta_\Xi$	> 0.981	> 0.9992
$r(\Xi^-)$	$0.2 < r(\Xi^-) < 100$ cm	$0.2 < r(\Xi^-) < 100$ cm
$ M_{\Lambda\pi} - m_\Xi $	$< 7 \text{ MeV}/c^2$	$< 7 \text{ MeV}/c^2$

Table 7: Topological and track selection criteria.

302 In the analysis of Ξ^{*0} , Λ and π from Ξ^- were selected with a DCA of less than 1.9 cm
 303 and with a DCA_r to the PV greater than 0.015 cm. The Λ daughter particles (π and p)
 304 were required to have a DCA_r to the PV greater than 0.06 cm, while the DCA between the
 305 two particles was required to be less than 1.4 cm. Cuts on the invariant mass, the cosine

³⁰⁶ of the pointing angle ($\theta_{\Lambda}, \theta_{\Xi}$) and the radius of the fiducial volume ($r(\Lambda), r(\Xi)$) in Table 7
³⁰⁷ were applied to optimize the balance of purity and efficiency of each particle sample.

308 **5.1.3 Particle identification**

309 PID selection criteria are applied for

- 310 1. π^\pm (last emitted π) and proton from Λ
- 311 2. π^\pm (second emitted π) from Ξ^\pm
- 312 3. π^\pm (first emitted π) from $\Xi(1530)^0$

313 by using TPC. On TPC dE/dx versus momentum distribution, 3σ cuts are applied to TPC
 314 for selecting each of the particles. The TPC dE/dx selection allows to have better signal
 315 with $\sim 20\%$ increase of significance.

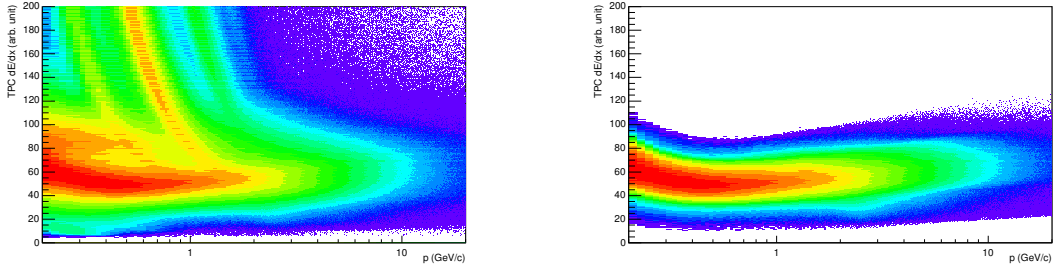


Figure 6: TPC dE/dx as function of transverse momentum for total (top) and selected first emitted π in 3σ (bottom)

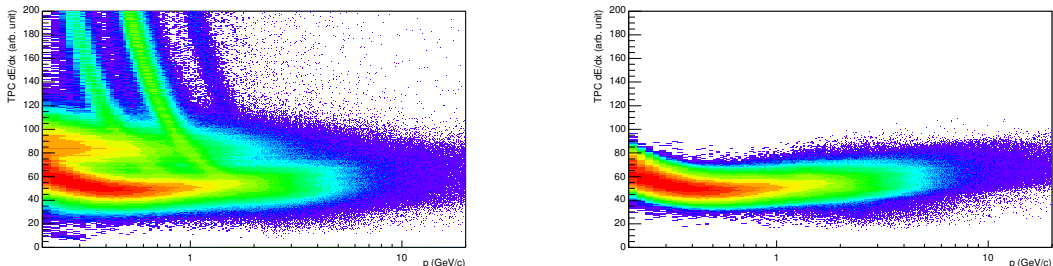


Figure 7: TPC dE/dx as function of transverse momentum for total (top) and selected second emitted π in 3σ (bottom)

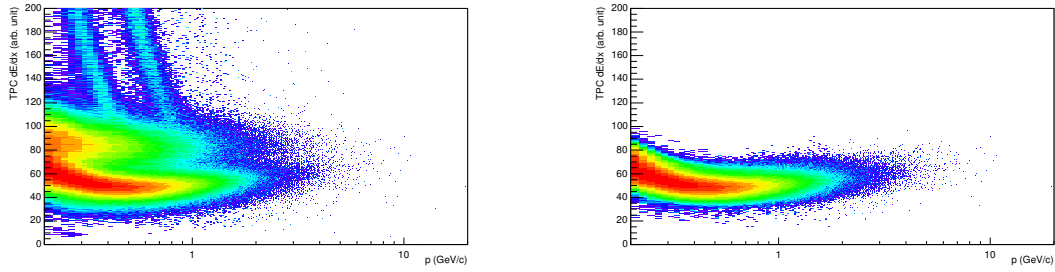


Figure 8: TPC dE/dx as function of transverse momentum for total (top) and selected last emitted π in 3σ (bottom)

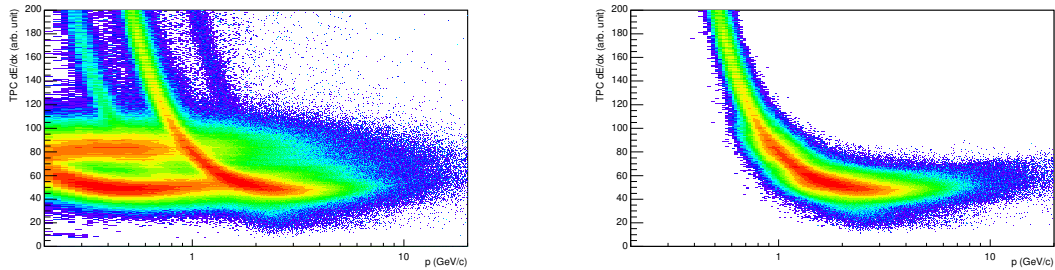


Figure 9: TPC dE/dx as function of transverse momentum for total (top) and selected proton in 3σ (bottom)

316 **5.1.4 Signal extraction**

317 The Ξ^{*0} signals were reconstructed by invariant-mass analysis of candidates for the decay
 318 products in each transverse momentum interval of the resonance particle, and for each
 319 multiplicity class. The $\Xi^-\pi^+(\Xi^+\pi^-)$ invariant mass distribution is reported in Figure 5.1.4
 320 for semi-central events (20-40%) in p–Pb collisions and Figure 5.1.4 for central events(0-
 321 10%) in Pb–Pb collisions.

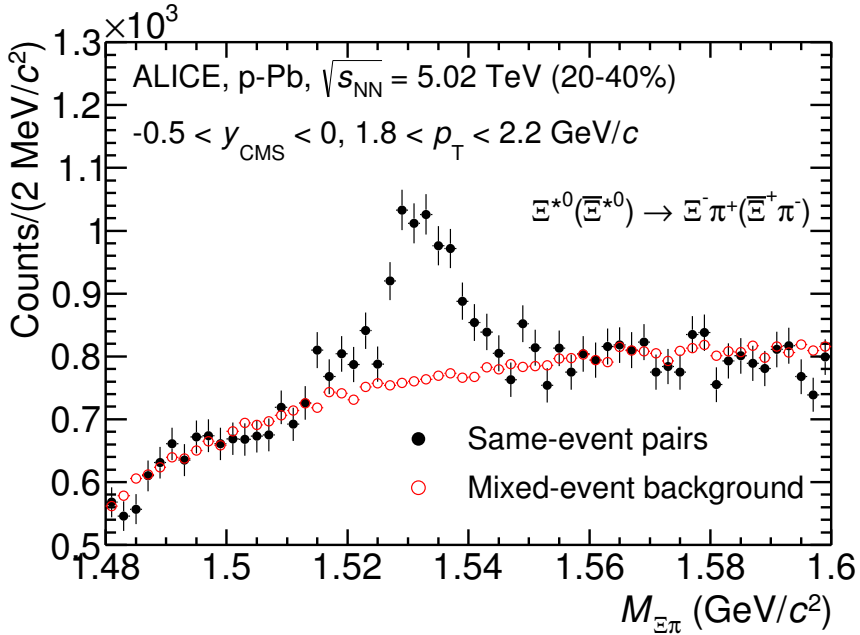


Figure 10: The $\Xi^\mp\pi^\pm$ invariant mass distribution (Same-event pairs) in $1.8 < p_T < 2.2$ GeV/ c and for the multiplicity class 20-40%. The background shape, using pairs from different events (Mixed-event background), is normalised to the counts in $1.49 < M_{\Xi\pi} < 1.51$ GeV/ c^2 and $1.56 < M_{\Xi\pi} < 1.58$ GeV/ c^2 .

322 Since the resonance decay products originate from a position which is indistinguishable
 323 from the PV, a significant combinatorial background is present. In order to extract
 324 $\Xi(1530)^0$ signal it is necessary to remove or, at least reduce, the combinatorial background.
 325 For this analysis, this has been done with the event mixing (EM) technique, by combining
 326 uncorrelated decay products 20 different events in p–Pb (5 different events in Pb–Pb). The
 327 events for the mixing have been selected by applying the similarity criteria to minimise
 328 distortions due to different acceptances and to ensure a similar event structure, only tracks
 329 from events with similar vertex positions z ($|\Delta z| < 1$ cm) and track multiplicities n ($|\Delta n| <$
 330 10) were taken.

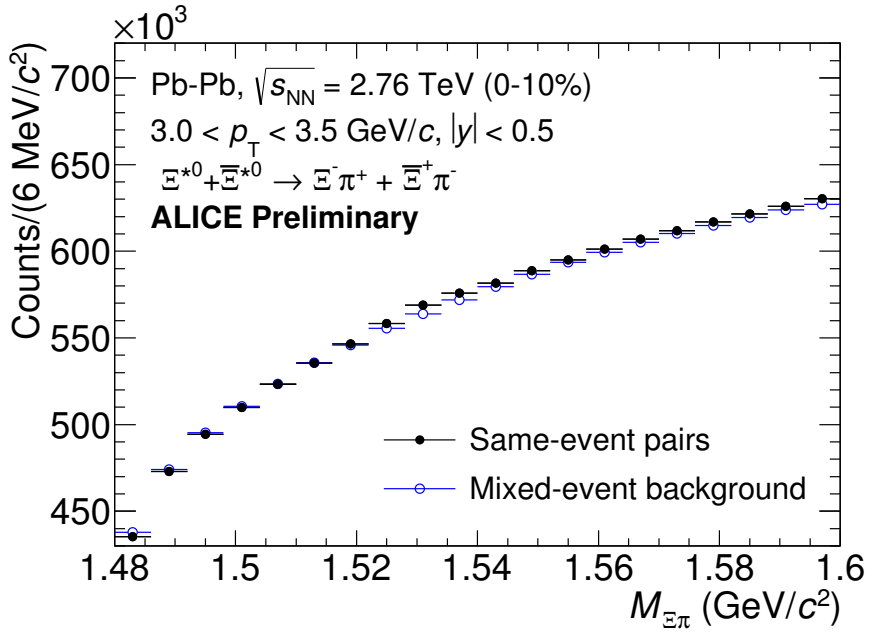


Figure 11: The $\Xi^\pm\pi^\pm$ invariant mass distribution (Same-event pairs) in $3.0 < p_T < 3.5 \text{ GeV}/c$ and for the centrality class 0-10%. The background shape, using pairs from different events (Mixed-event background), is normalised to the counts in $1.49 < M_{\Xi\pi} < 1.51 \text{ GeV}/c^2$ and $1.56 < M_{\Xi\pi} < 1.58 \text{ GeV}/c^2$.

331 The mixed-event background distributions were normalised to two fixed regions,
 332 $1.49 < M_{\Xi\pi} < 1.51 \text{ GeV}/c^2$ and $1.56 < M_{\Xi\pi} < 1.58 \text{ GeV}/c^2$, around the Ξ^{*0} mass
 333 peak (Figure 5.1.4 and 5.1.4). These regions were used for all p_T intervals and multiplicity
 334 classes, because the background shape is reasonably well reproduced in these regions and
 335 the invariant-mass resolution of the reconstructed peaks appears stable, independently of
 336 p_T . The uncertainty on the normalisation was estimated by varying the normalisation
 337 regions and is included in the quoted systematic uncertainty for the signal extraction (Sec-
 338 tion 5.4).

339 After the background subtraction, the resulting distribution is shown in Figure 5.1.4
 340 and 5.1.4. In order to obtain raw yields, a combined fit of a first-order polynomial for
 341 the residual background and a Voigtian function (a convolution of a Breit-Wigner and a
 342 Gaussian function accounting for the detector resolution) for the signal was used. The
 343 mathematical form of fit function used in analysis is:

$$f(M_{\Xi\pi}) = \frac{Y}{2\pi} \frac{\Gamma_0}{(M_{\Xi\pi} - M_0)^2 + \frac{\Gamma_0^2}{4}} \frac{e^{-(M_{\Xi\pi} - M_0)/2\sigma^2}}{\sigma\sqrt{2\pi}} + bg(M_{\Xi\pi}) \quad (1)$$

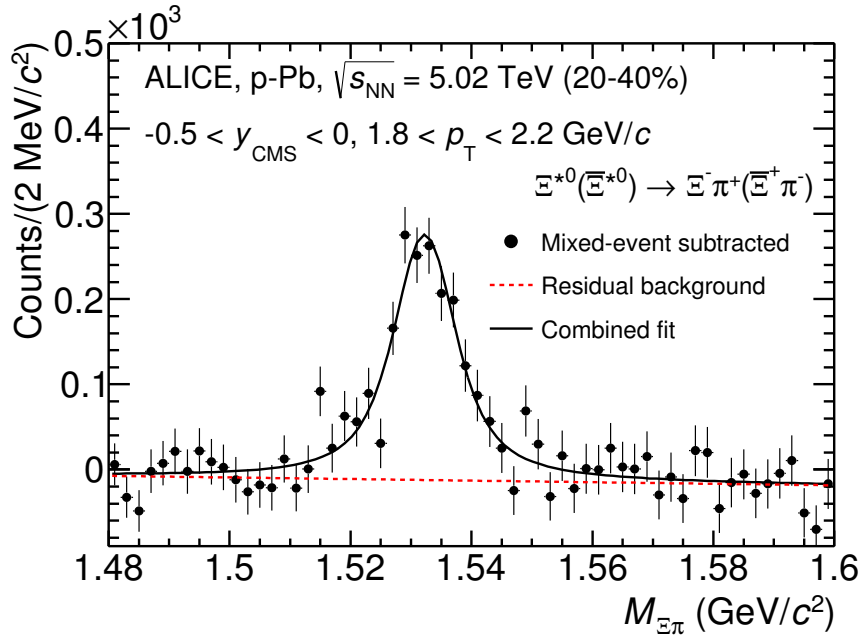


Figure 12: The invariant mass distribution after subtraction of the mixed-event background in p–Pb collisions. The solid curve represents the combined fit, while the dashed line describes the residual background.

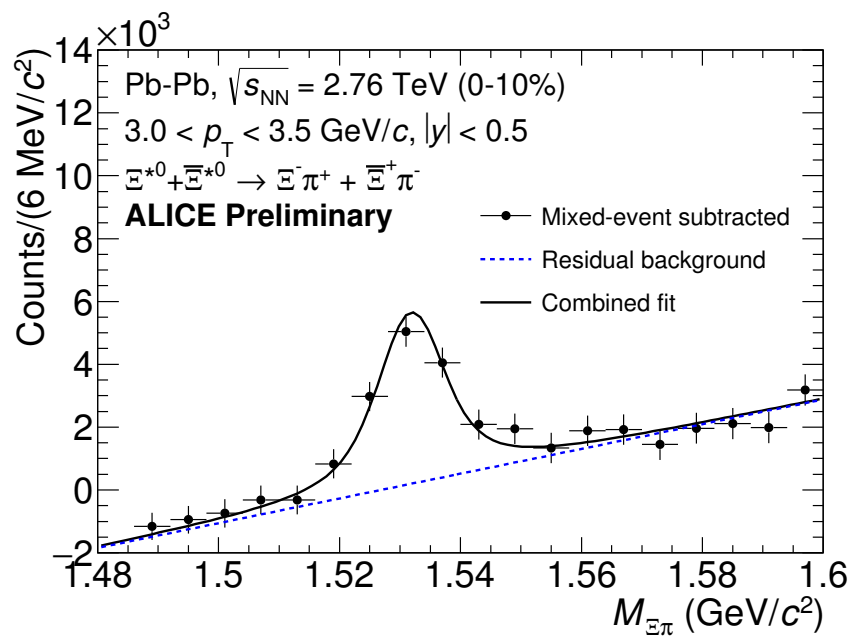


Figure 13: The invariant mass distribution after subtraction of the mixed-event background in Pb–Pb collisions. The solid curve represents the combined fit, while the dashed line describes the residual background.

344 The mass parameter of the Voigtian fit (M_0) is left free within the fit range ($1.48 \text{ GeV}/c^2$
345 and $1.59 \text{ GeV}/c^2$). The overall invariant mass width of the Voigtian function is governed
346 by 2 parameters: σ and Γ_0 . The σ describes the broadening of the peak due to finite
347 detector resolution while Γ describes the intrinsic width of the resonance itself. The Γ_0 is
348 fixed to the PDG value of $9.1 \text{ MeV}/c$ for the $\Xi(1530)^0$. Because of lack of statistics, the
349 σ can be over estimated. Therefore the σ parameter is fixed to value derived from σ in
350 MB events which has largest statistics. The σ as function of p_T distribution in MB events
351 is shown in Figure. 14 and we also report invariant mass of $\Xi(1530)^0$ as function of p_T in
352 Figure. 15. The $\Xi(1530)^0$ raw yields have been extracted from the fit for the 4 multiplicity
353 bins (+1NSD events) in p–Pb and 4 centrality bins in Pb–Pb collisions and the yields as
354 function of p_T are shown in Figure 16.

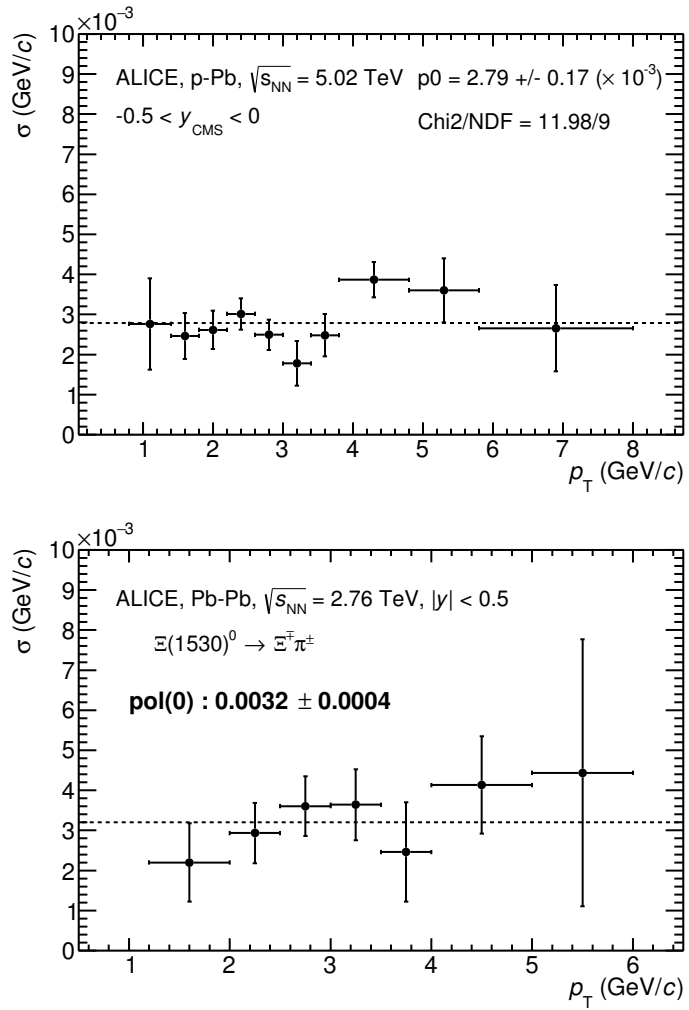


Figure 14: σ fit parameters as a function of p_T in MB in p–Pb collisions (top) and in Pb–Pb collisions (bottom).

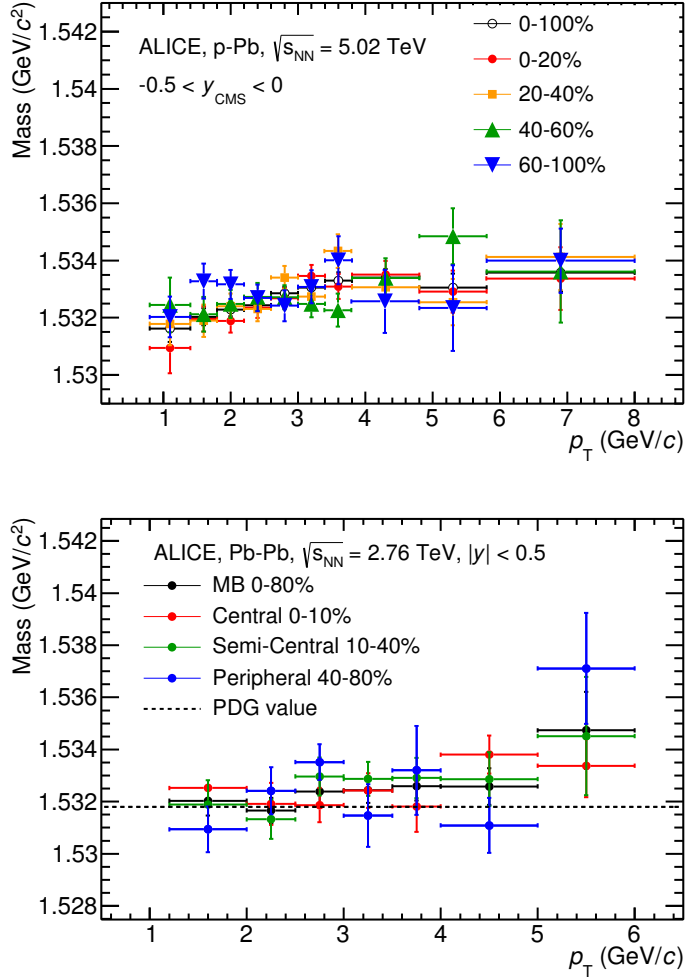


Figure 15: $\Xi(1530)^0$ -mass obtained from fit of the Voigtian peak as a function of p_T in each multiplicity classes in p-Pb collisions (top) and the different centrality classes in Pb-Pb (bottom).

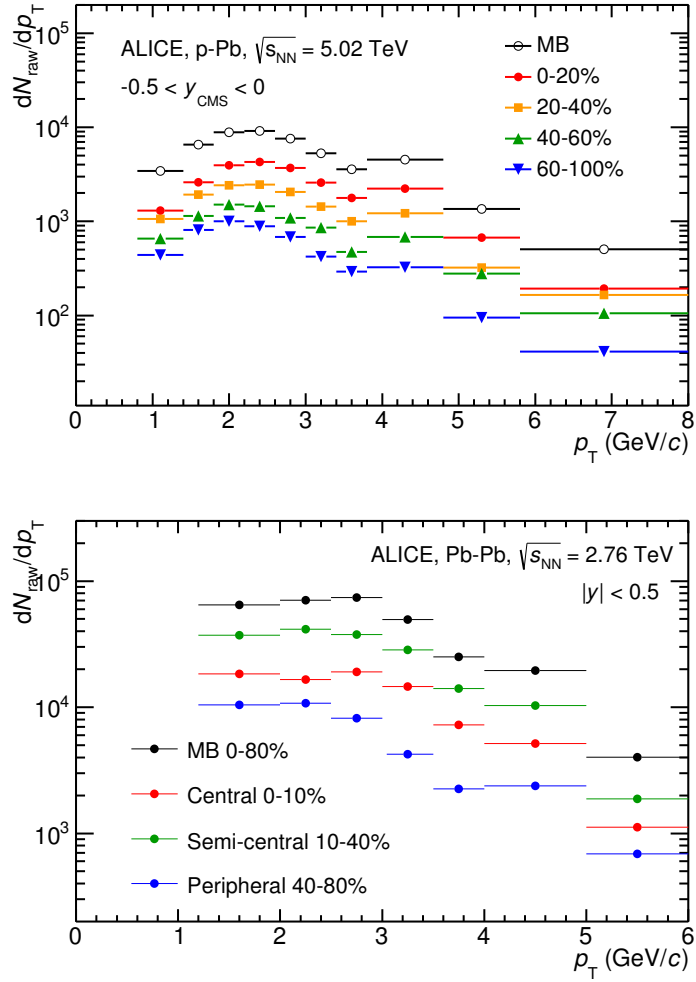


Figure 16: $\Xi(1530)^0$ -raw spectra obtained from fit of the Voigtian peak and a polynomial residual background for different multiplicities in p-Pb collisions (top) and Pb-Pb collisions (bottom). Only the statistical error is reported.

355 **5.2 Efficiency correction**

356 The raw yields were corrected for the geometrical acceptance and the reconstruction effi-
 357 ciency ($A \times \epsilon$) of the detector (Figure. 17). By using the DPMJET 3.05 event generator [13]
 358 and the GEANT 3.21 package [14], a sample of about 100 million p–Pb events was sim-
 359 ulated and reconstructed in order to compute the corrections. The distributions of $A \times \epsilon$
 360 were obtained from the ratio between the number of reconstructed Ξ^{*0} and the number of
 361 generated particle in the same p_T and rapidity interval. Since the correction factors for
 362 different multiplicity classes are in agreement with those from MB events within statistical
 363 uncertainty, the latter were used for all multiplicity classes.

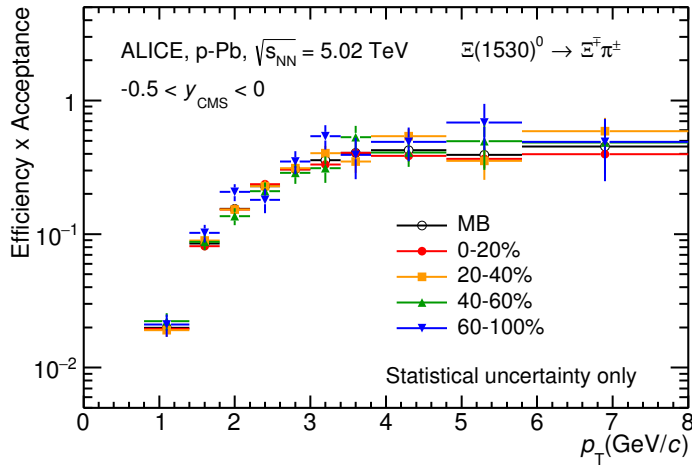


Figure 17: $\Xi(1530)^0$ -raw spectra obtained from fit of the Voigtian peak and a polynomial residual background for different multiplicities. Only the statistical error is reported.

364 Because the generated $\Xi(1530)^0$ spectra have different shapes than the measured $\Xi(1530)^0$
 365 spectra, it is necessary to weight the generated and reconstructed $\Xi(1530)^0$ spectra in these
 366 simulations. Fig. 18 shows the generated and reconstructed $\Xi(1530)^0$ spectra plotted with
 367 the (corrected) measured $\Xi(1530)^0$ spectrum for MB events and the Levy fit of that mea-
 368 sured spectrum. The generated and measured $\Xi(1530)^0$ spectra have different behaviours
 369 for the range $0.5 < p_T < 1$ GeV/ c . The generated $\Xi(1530)^0$ spectrum decreases with
 370 increasing p_T over this range, while the fit of the measured $\Xi(1530)^0$ spectrum reaches a
 371 local maximum in this range. The correction ϵ is observed to change rapidly over this
 372 p_T range. It is therefore necessary to weight the generated spectrum so that it has the
 373 shape of the measured $\Xi(1530)^0$ spectrum (and to apply corresponding weights to the re-
 374 constructed $\Xi(1530)^0$ spectrum). An iterative procedure is performed to determine the
 375 correct weighting (and therefore the correct ϵ).

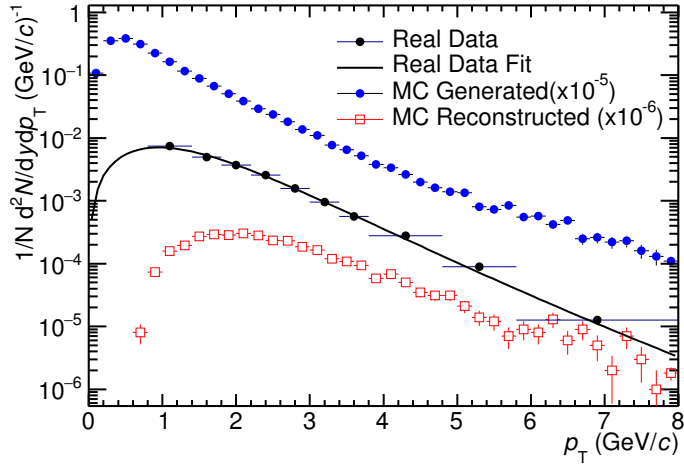


Figure 18: Real corrected $\Xi(1530)^0$ spectrum (black) for the minimum bias with Levy fit (black curve). Also shown are the unweighted generated (blue) and reconstructed (red) $\Xi(1530)^0$ spectra.

- 376 1. The unweighted ϵ is calculated.
- 377 2. This ϵ is used to correct the measured xis spectrum.
- 378 3. The corrected $\Xi(1530)^0$ spectrum is fit.
- 379 4. This fit is used to weight the simulated xis spectra. A p_T dependent weight is applied
380 to the generated xis spectrum so that it follows the fit. The same weight is applied
381 to the reconstructed xis spectrum.
- 382 5. The (weighted) ϵ is calculated.
- 383 6. Steps 2-5 are repeated (with the weighted ϵ from step 5 used as the input for step 2)
384 until the ϵ values are observed to change by $< 0.1\%$ (relative) between iterations. It
385 is observed that four iterations are sufficient for this procedure to converge.

386 Finally, the re-weighted efficiency is obtained and the distribution as function of p_T is
387 shown in Figure 19.

388 In order to obtain the correction factor dedicated in Pb-Pb collisions, MC events are
389 generated using Heavy Ion Jet Interaction Generator (HIJING). The generated events are
390 passed through a GEANT3 model of the ALICE experiment with a realistic description of
391 the detector response. Because we have observed centrality dependent efficiency, the cen-
392 trality dependent efficiencies have been applied to get corrected raw yield. The reweighting

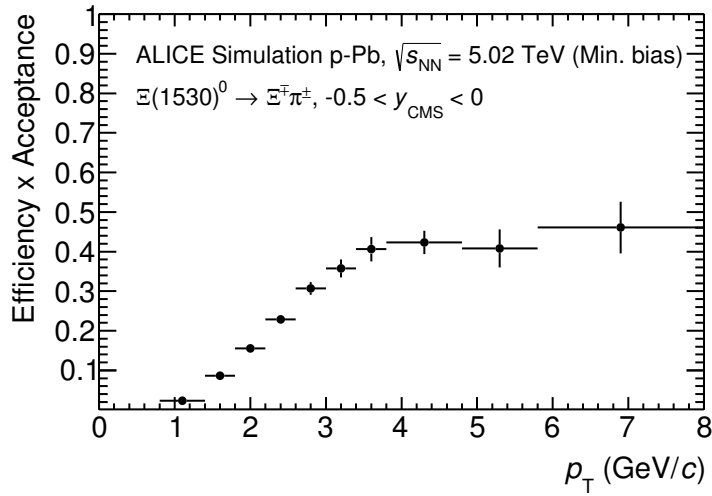


Figure 19: Efficiency as a function of p_T in minimum bias events in p–Pb collisions.

393 approach which was used to correct the efficiency in p–Pb is also applied to the efficiency
 394 obtained in Pb–Pb.

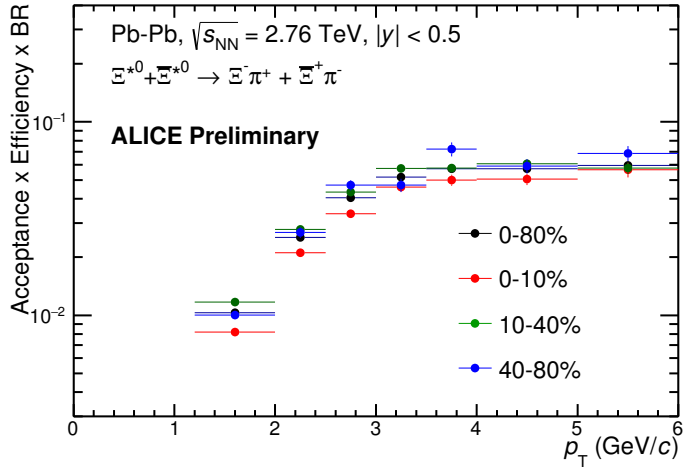


Figure 20: Efficiency as a function of p_T in different centrality classes in Pb–Pb collisions

395 5.3 Corrected p_T -spectra

396 The p_T spectrum is by the number of produced particles of a given type in the desired
 397 interval of phase-space divided by the number of inelastic collisions. The spectrum is
 398 calculated as:

$$\frac{1}{N} \times \frac{d^2N}{dydp_T} = \frac{1}{N_{E,PhysSel}} \times \frac{N_{raw}}{dp_T dy} \frac{1}{\epsilon} \frac{N_{total}^{MC}}{N_{post-PVcut}^{MC}}, \quad (2)$$

399 where N_E represent the number inelastic collisions, the $\frac{dN}{dydp_T}$ is the yield per range of
 400 rapidity y , per range in p_T . On the right hand side $N_{E,PhysSel}$ is the number of events
 401 counted by the physics selection trigger. N_{raw} is the raw extracted number of particle in the
 402 rapidity and p_T bin of width $\Delta y = 0.5$ in p–Pb ($\Delta y = 1.0$ in Pb–Pb) and Δp_T , respectively.
 403 ϵ is the reconstruction efficiency estimated from Monte Carlo simulations. $\frac{N_{total}^{MC}}{N_{post-PVcut}^{MC}}$ is the
 404 ratio of the total number of particle from MC divided by the number of particle from MC
 405 after the Primary-Vertex cut is imposed. It takes into account the fraction of particle lost
 406 after imposing the PV cut. We notice that for minimum-bias results in p–Pb, we adopted
 407 a normalisation such that to provide result from non-single diffractive(NSD) cross-section.
 408 The normalisation factor is 0.964 [6]. The obtained spectrum at MB and the spectrums
 409 from different multiplicity classes in p–Pb are shown in Figure 21 and different centrality
 410 classes in Pb–Pb are shown in Figure 22.

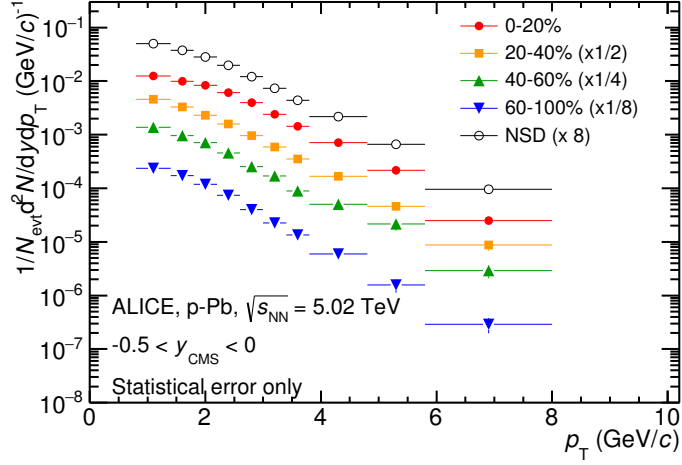


Figure 21: Corrected p_T -spectra of $\Xi(1530)^0$ in NSD and different multiplicity classes in p-Pb collisions.

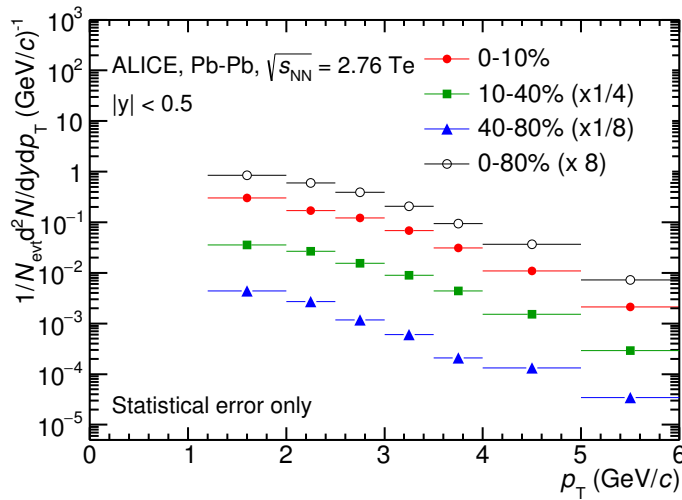


Figure 22: Corrected p_T -spectra of $\Xi(1530)^0$ in different centrality classes in Pb-Pb collisions.

411 **5.4 Systematic uncertainties**

412 The systematic uncertainties are calculated in seven principle groups. The procedure to ob-
 413 tain the systematic uncertainties is performed many times by varying the possible permuta-
 414 tion of the analysis parameter. The general strategy for evaluating systematic uncertainties
 415 is described as following:

- 416 1. Choose one set of parameters for the analysis as default
- 417 2. Observe the deviation of yield when one parameter is changed
- 418 3. The systematic uncertainty is calculated for a given source as the RMS deviation of
 the available sources.
- 420 4. The total systematic uncertainty, taking into account all the different sources, is the
 sum in quadrature of each source.

422 To study the systematic effect we repeat the measurement by varying one parameter at
 423 a time. A Barlow [15] check has been performed for each measurement to verify whether it
 424 is due to a systematic effect or a statistical fluctuation. Let each measurement be indicated
 425 by $(y_i \pm \sigma_i)$ and the central value (default measurement) by $(y_c \pm \sigma_c)$, one can define $\Delta\sigma_i$
 426 (Eq. 3).

$$\Delta\sigma_i = \sqrt{(\sigma_i^2 - \sigma_c^2)} \quad (3)$$

427 Then we calculate $n_i = \Delta y_i / \Delta\sigma_i$, where $\Delta y_i = |y_c - y_i|$. If $n_i \leq 1.0$ then the effects
 428 are due to the statistical fluctuation and if $n_i > 1.0$ we apply consistency check. Since
 429 the alternate and default measurements are not statistically independent, an alternate
 430 measurement which is statistically consistent with the default measurement should not be
 431 used in calculating a systematic uncertainty. The difference between the two measurements
 432 is $\Delta = y_c - y_i$. The difference in quadrature of the uncertainties is calculated by Eq. 3. It
 433 could be possible to check if $\Delta < \sigma$ and exclude such cases from the systematic uncertainties.
 434 However, there can be statistical fluctuations for which $\Delta > \sigma$. If the variations between the
 435 default and alternate measurements are purely statistical, the distribution of Δ/σ should
 436 be a Gaussian with a mean value that is consistent with zero and a deviation σ consistent
 437 with unity. In this analysis, if the mean value is less than 0.1 and σ is less than 1, the
 438 variation passes the consistency check.

439 Only the measurements which passed the Barlow check ($n_i > 1$) are used to determine
 440 the systematic uncertainty. For measurements $N > 2$, the systematic uncertainty has been
 441 determined as the RMS (eqn. 4) of the available measurements. If $N=2$, the absolute
 442 difference is assigned as systematic uncertainty.

$$\delta y_{syst.} = \sqrt{\frac{1}{N} \sum_i (y_i - \bar{y})^2} \quad (4)$$

443 Here N is the total number of available measurements including y_c and \bar{y} is the average
444 of value of the measurements. The measurement did not pass Barlow check, zero systematic
445 uncertainty has been assigned to the value.

446 By suing the way as explained above, all the main contributions to the systematic un-
447 certainty of particle spectra have been studied. In particular those that comes from signal
448 extraction, topological and kinematical selection cuts, track quality selection and $n\sigma$ TPC
449 PID variation. the meaning of each source of systematic uncertainty studied is described
450 in the following:

451

452 **Signal extraction**

453 We have extracted the signal with varying the yield calculating method which contains
454 the method of signal extraction by integrating the Voigtian fit function and bin counting.
455 We also have varied the normalisation range which is related to the invariant mass region
456 where the mixed events distribution is scaled to subtract the combinatorial background
457 and different background estimator such as Like-Sign distribution and polynomial fit was
458 taken account into the systematic source of signal extraction. The systematic uncertainty
459 from signal extraction is sum in quadrature of three sources.

460

461 **Topological selection**

462 To evaluate the stability of the chosen set of values for the topological cuts, loose and tight
463 cuts have beed defined in order to vary by $\pm 10\%$ respectively. The parameters are changed
464 once at a time. Total systematic uncertainty from topological selection is calculated by
465 summation in quadrature of nine sources.

466

467 **TPC $N_{cluster}$ selection**

468 The selection performed for the daughter tracks of the cascade is that $N_{cluster}$ is larger
469 than 70 and the value has been varied to 60 and 80 in order to estimate the systematic
470 uncertainty due to this selection.

471

472 **TPC dE/dx selection**

473 In order to evaluate any potential effect due to the TPC dE/dx selection (U_{PID}), the N_σ
474 selection was varied with $N = 2.5$ and 3.5 .

475

476 **p_T shape correction**

477 As described in Section 5.2, due to the different shape of the measured and generated
478 $\Xi(1530)^0$ spectra, we have applied reweighing procedure to the generated spectra to have
479 same shape and this correction is added into contributor of systematic uncertainty as
480 p_T shape correction.

481

482 **Mass window range selection**

483 In order to select Ξ^\pm which is daughter particle of $\Xi(1530)^0$, we apply the mass window

484 ± 7 MeV/ c^2 around $\Xi(1530)^0$ mass on $\Lambda\pi$ invariant mass distribution. The boundaries
485 has been varied to ± 6 MeV/ c^2 and ± 8 MeV/ c^2 to estimate systematic uncertainty.

486

487 **Vertex range selection**

488 The distribution of vertex-z is shown in Fig.3. The cut on |Vz| was varied from the nominal
489 ± 10 cm to ± 9 cm, ± 11 cm.

490

491 **Material Budget and hadronic cross section**

492 A possible source of uncertainty comes from the description of the material, active (de-
493 tecting area) or dead (structure and cable), that the particles cross during their travel in
494 the MC with respect to the real material present in the detector. Such description could
495 affect the reconstruction efficiency in different aspects (e.g. multiple scattering, energy
496 loss). The value estimated by Ξ analysis [16] has been used in this study which gives 4%
497 systematic uncertainty. In case of systematic uncertainty from hadronic cross section, we
498 have inherited the value studied in previous measurement[17] which amount is 1%.

499

500 **Tracking efficiency**

501 Systematic uncertainties from tracking efficiency from ITS + TPC combined track were
502 assigned as 3% in p–Pb and 4% in Pb–Pb collision system.[17]
503 (<https://twiki.cern.ch/twiki/bin/view/ALICE/TrackingEfficiencyCharged>)

504

505 Finally, total systematic uncertainty is sum in quadrature of sources listed above. Fig-
506 ure 23 and Figure 24 show the total systematic uncertainty in minimum bias event and
507 different multiplicity classes in p–Pb collisions, respectively. Again, Figure 25 and Figure
508 26 present the total systematic uncertainty in minimum bias event and different centrality
509 classes in Pb–Pb collisions.

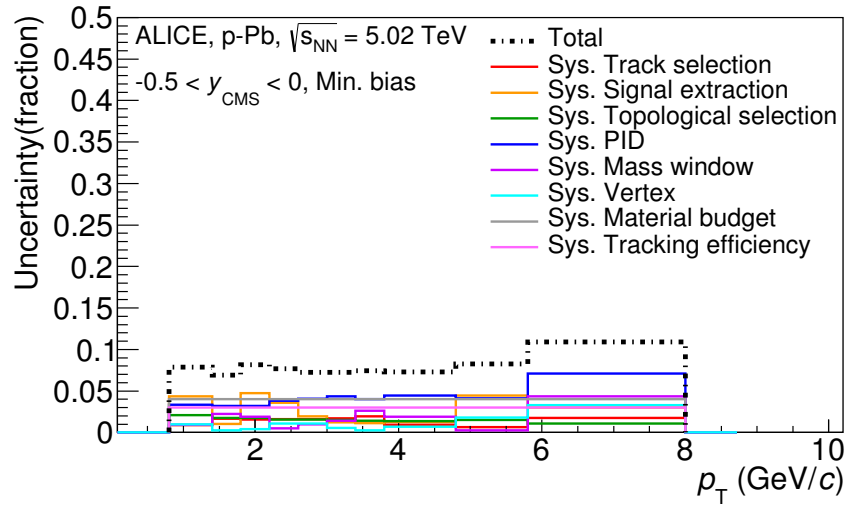


Figure 23: Summary of the contributions to the systematic uncertainty in minimum bias events in p–Pb collisions. The dashed black line is the sum in quadrature of all the contributions.

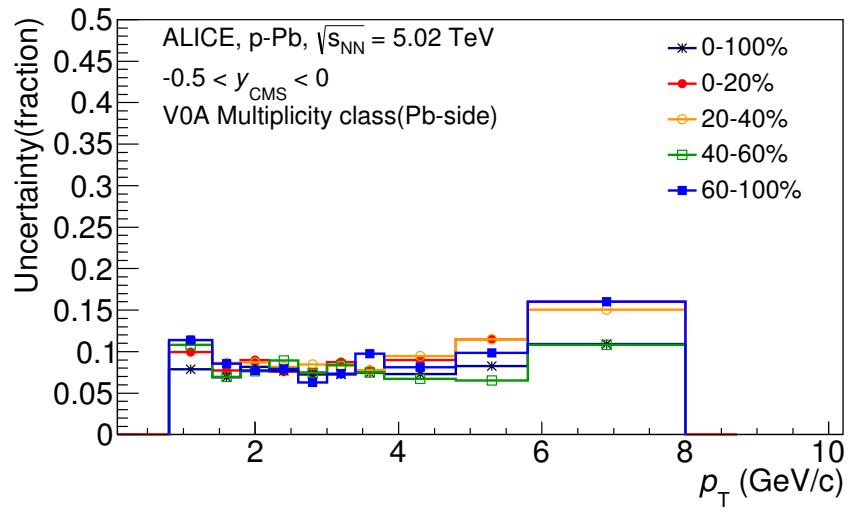


Figure 24: Systematic uncertainties for each multiplicity classes in p–Pb collisions.

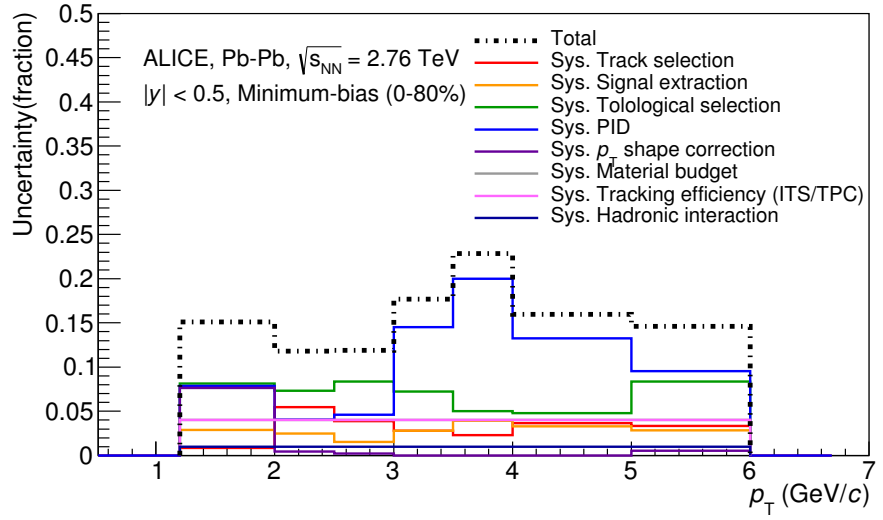


Figure 25: Summary of the contributions to the systematic uncertainty in minimum bias events in Pb–Pb collisions. The dashed black line is the sum in quadrature of all the contributions.

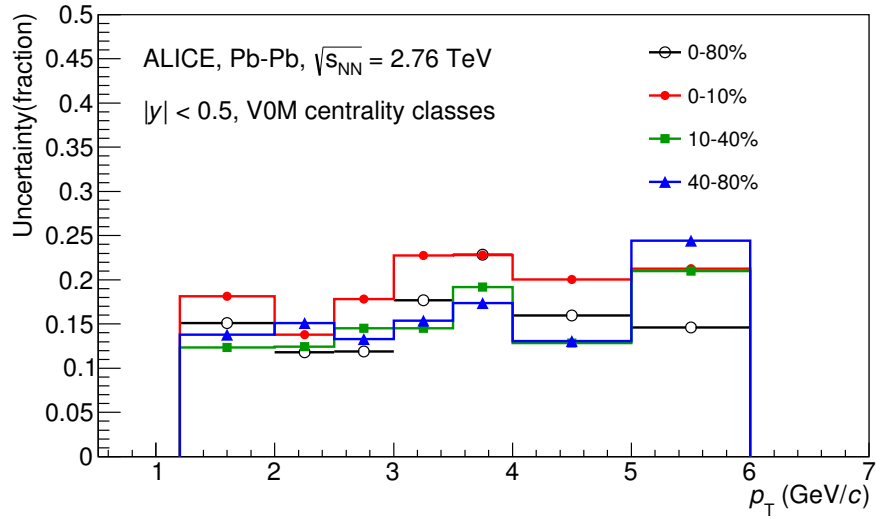


Figure 26: Systematic uncertainties for each multiplicity classes.

Source of uncertainty	$\Xi(1530)^0$ in p-Pb	$\Xi(1530)^0$ in Pb-Pb
<i>p_T-dependent</i>		
Tracking efficiency	3%	4%
Tracks selection	1-2%	1-5%
Topological selection	1-2%	5-8%
PID	3-7%	4-20%
Signal extraction	1-5%	1-4%
<i>p_T</i> shape correction	-	0-8%
Mass window (Ξ^{\pm})	4	-
Vertex selection	3%	-
<i>p_T-independent</i>		
Hadronic interaction	-	1%
Material budget	4%	4%
Branching ratio	0.3%	0.3%
Total	8-12%	9-25 %

Table 8: Summary of the systematic uncertainties on the differential yield, $d^2N/(dp_T dy)$. Minimum and maximum values in all p_T intervals and multiplicity classes in p–Pb, centrality classes in Pb–Pb are shown for each source.

510 5.5 $\Xi(1530)^0$ transverse momentum spectra

511 The raw yield shown in Figure 21 and 22 have been corrected for efficiency as described
 512 in section 5.2. The measured spectra for $(\Xi(1530)^0 + \bar{\Xi}(1530)^0)/2$ are reported in Figure
 513 27 for p–Pb collisions and Figure 28 for Pb–Pb collisions. The statistical and systematic
 514 uncertainties are reported respectively as the error bars and the boxes on the plot. The
 515 corrected yields for p–Pb collisions are measured with $0.8 < p_T < 8.0$ GeV/c while the
 516 yields for Pb–Pb collisions are obtained with $1.2 < p_T < 6.0$ GeV/c due to difficulty of
 517 signal extraction in low and high p_T region.

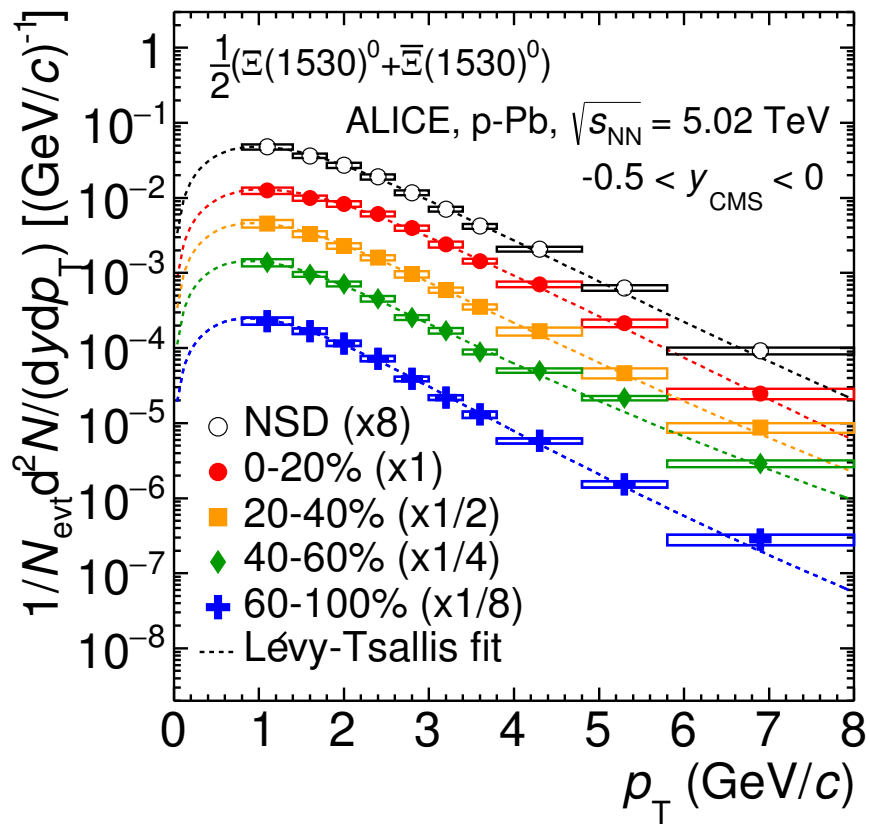


Figure 27: Corrected yields as function of p_T in NSD events and multiplicity dependent event classes in p-Pb collision system. Statistical uncertainties are presented as bar and systematical uncertainties are plotted as boxes.

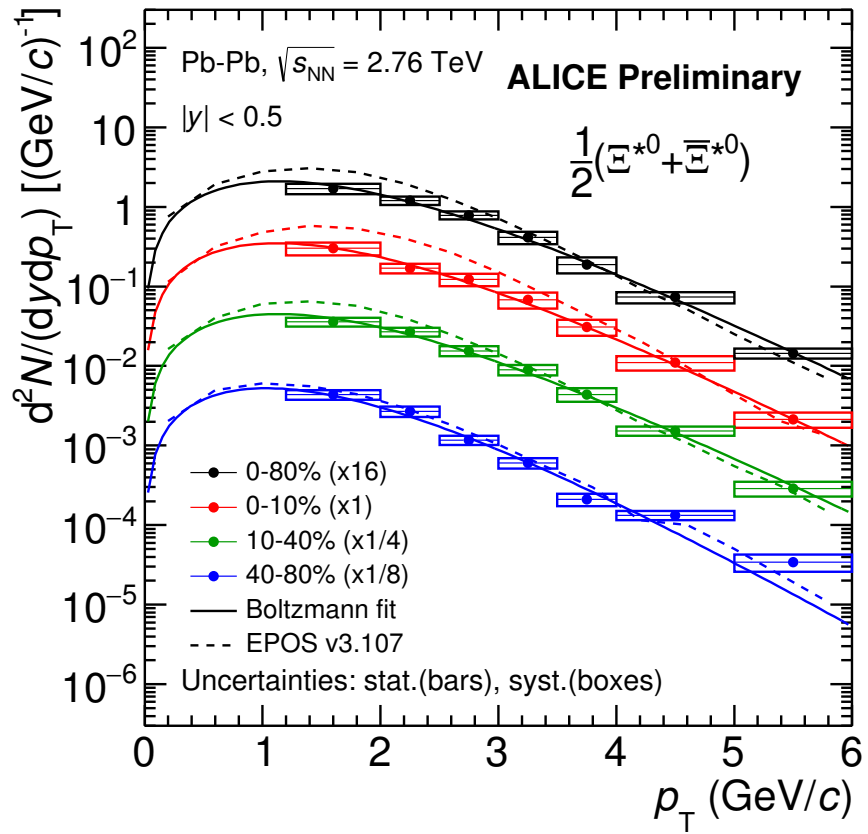


Figure 28: Corrected yields as function of p_T in different centrality classes in Pb–Pb collision system. Statistical uncertainties are presented as bar and systematical uncertainties are plotted as boxes.

518 **6 Results**

519 **6.1 dN/dy and $\langle p_T \rangle$**

520 **6.2 Particle yield ratios**

521 **6.2.1 Comparison with other resonances**

522 **6.2.2 Comparison with models**

523 **References**

- [1] D. Hahn and H. Stoecker, “THE QUANTUM STATISTICAL MODEL OF FRAGMENT FORMATION: ENTROPY AND TEMPERATURE EXTRACTION IN HEAVY ION COLLISIONS,” *Nucl. Phys.* **A476** (1988) 718–772.
- [2] S. Wheaton, J. Cleymans, and M. Hauer, “THERMUS: A Thermal model package for ROOT,” *Comput. Phys. Commun.* **180** (2009) 84–106, [hep-ph/0407174](#).
- [3] J. Cleymans, S. Kabana, I. Kraus, H. Oeschler, K. Redlich, and N. Sharma, “Antimatter production in proton-proton and heavy-ion collisions at ultrarelativistic energies,” *Phys. Rev.* **C84** (2011) 054916, [arXiv:1105.3719 \[hep-ph\]](#).
- [4] **ALICE** Collaboration, K. Aamodt *et al.*, “The ALICE experiment at the CERN LHC,” *JINST* **3** (2008) S08002.
- [5] **ALICE** Collaboration, B. Abelev *et al.*, “Performance of the ALICE Experiment at the CERN LHC,” *Int. J. Mod. Phys.* **A29** (2014) 1430044, [arXiv:1402.4476 \[nucl-ex\]](#).
- [6] **ALICE** Collaboration, J. Adam *et al.*, “Production of $K^*(892)^0$ and $\phi(1020)$ in $p\text{-Pb}$ collisions at $\sqrt{s_{NN}} = 5.02$ TeV,” *Eur. Phys. J.* **C76** (2016) 245, [arXiv:1601.7868 \[nucl-ex\]](#).
- [7] **ALICE** Collaboration, B. Abelev *et al.*, “Pseudorapidity Density of Charged Particles in $p\text{-Pb}$ Collisions at $\sqrt{s_{NN}} = 5.02$ TeV,” *Phys. Rev. Lett.* **110** (2013) 032301, [arXiv:1210.3615 \[nucl-ex\]](#).
- [8] **ALICE** Collaboration, B. Abelev *et al.*, “Centrality determination of Pb-Pb collisions at $\sqrt{s_{NN}} = 2.76$ TeV with ALICE,” *Phys. Rev.* **C88** (2013) , [arXiv:1303.0737 \[nucl-ex\]](#).
- [9] **ALICE** Collaboration, B. Abelev *et al.*, “Production of $\Sigma(1385)^{\pm}$ and $\Xi(1530)^0$ in proton-proton collisions at $\sqrt{s} = 7$ TeV,” *Eur. Phys. J.* **C75** (2015) 1, [arXiv:1406.3206 \[nucl-ex\]](#).

- 549 [10] **Particle Data Group** Collaboration, K. Olive *et al.*, “Review of Particle Physics,”
 550 *Chin. Phys. C***38** (2014) 090001.
- 551 [11] **ALICE** Collaboration, J. Adam *et al.*, “Multi-strange baryon production in p–Pb
 552 collisions at $\sqrt{s_{\text{NN}}}=5.02$ TeV,” *Phys. Lett. B***758** (2016) 389–401,
 553 [arXiv:1512.07227](https://arxiv.org/abs/1512.07227) [nucl-ex].
- 554 [12] **ALICE** Collaboration, K. Aamodt *et al.*, “Strange particle production in
 555 proton-proton collisions at $\sqrt{s}=0.9$ TeV with ALICE at the LHC,” *Eur. Phys. J.*
 556 *C***71** (2011) 1594, [arXiv:1012.3257](https://arxiv.org/abs/1012.3257) [nucl-ex].
- 557 [13] S. Roesler, R. Engel, , and J. Ranft, “The Monte Carlo Event Generator
 558 DPMJET-III, Advanced Monte Carlo for Radiation Physics, Particle Transport
 559 Simulation and Applications,” *Conference Proceedings, MC2000, Lisbon, Portugal,*
 560 *October 23–26* (2000) 1033–1038, [hep-ph/0012252](https://arxiv.org/abs/hep-ph/0012252).
- 561 [14] R. Brun, F. Carminati, and S. Giani, “GEANT detector description and simulation
 562 tool,” *CERN-W5013* (1994) .
- 563 [15] R. Barlow, “Systematic Errors: Facts and Fictions,” *Presented at Advanced*
 564 *Statistical Techniques in HEP, Durham, March 2002* (2002) 333p,
 565 [hep-ex/0207026v1](https://arxiv.org/abs/hep-ex/0207026v1).
- 566 [16] **ALICE** Collaboration, B. Abelev *et al.*, “Multi-strange baryon production at
 567 mid-rapidity in Pb–Pb collisions at $\sqrt{s_{\text{NN}}}=2.76$ TeV,” *Phys. Lett. B***728** (2014)
 568 216–227, [arXiv:1307.5543](https://arxiv.org/abs/1307.5543) [nucl-ex].
- 569 [17] **ALICE** Collaboration, B. Abelev *et al.*, “Centrality dependence of π , K and p
 570 production in Pb–Pb collisions at $\sqrt{s_{\text{NN}}}=2.76$ TeV,” *Phys. Rev. C***88** (2013) ,
 571 [arXiv:1301.4361](https://arxiv.org/abs/1301.4361) [nucl-ex].

572 **Acknowledgements**